APPLIED GEOPHYSICS, Vol.14, No.4 (December 2017), P. 463–479, 17 Figures.
DOI:10.1007/s11770-017-0640-y

Prediction of brittleness based on anisotropic rock physics model for kerogen-rich shale*

Qian Ke-Ran♦[1,2,3,4], He Zhi-Liang[1,2,3,4], Chen Ye-Quan[1,2,3,4], Liu Xi-Wu[1,2,3,4], and Li Xiang-Yang[5]

Abstract: The construction of a shale rock physics model and the selection of an appropriate brittleness index (*BI*) are two significant steps that can influence the accuracy of brittleness prediction. On one hand, the existing models of kerogen-rich shale are controversial, so a reasonable rock physics model needs to be built. On the other hand, several types of equations already exist for predicting the *BI* whose feasibility needs to be carefully considered. This study constructed a kerogen-rich rock physics model by performing the self-consistent approximation and the differential effective medium theory to model intercoupled clay and kerogen mixtures. The feasibility of our model was confirmed by comparison with classical models, showing better accuracy. Templates were constructed based on our model to link physical properties and the *BI*. Different equations for the *BI* had different sensitivities, making them suitable for different types of formations. Equations based on Young's Modulus were sensitive to variations in lithology, while those using Lame's Coefficients were sensitive to porosity and pore fluids. Physical information must be considered to improve brittleness prediction.
Keywords: Rock physics modeling, brittleness, shale, anisotropy

Introduction

Shale hydrocarbon reservoirs typically have low permeability and low porosity, so traditional exploration methods are insufficient to deal with most shale reservoirs. In order to obtain commercially viable production of hydrocarbons, oil companies often perform hydraulic fracturing to create artificial fractures and increase both permeability and porosity. This reduces the difficulty of exploration and enhances production (Goodway et al., 2010). Accurate prediction

Manuscript received by the Editor June 13, 2017; revised manuscript received October 15, 2017.
*This study is financially supported by the NSFC and Sinopec Joint Key Project (No. U1663207), National Science and Technology Major Project (No. 2017ZX05049-002), and National 973 Program (No. 2014CB239104).
1. National Key Laboratory of Corporation of Shale Oil/Gas enrichment mechanism and effective development, Beijing 100083, China.
2. National Energy R & D center of shale oil, Beijing 100083, China.
3. SinoPEC Key Laboratory of Shale Oil/Gas Exploration and Production Technology, Beijing 100083, China.
4. SinoPEC Petroleum Exploration and Production Research Institute, Beijing 100083, China.
5. China University of Petroleum (Beijing), State Key lab for Petroleum Resources and Prospecting, Beijing 102249, China.
♦Corresponding author: Qian Ke-Ran (Email: qiankeran@hotmail.com)

of the brittleness of the reservoir rock is essential for effective hydraulic fracturing, and three-dimensional (3D) elasticity measurements from geophysical data allow prediction of 3D brittleness.

The construction of a rock physics model and the selection of a suitable brittleness index (*BI*) equation are two key steps that may influence the accuracy of brittleness prediction. A rock physics model can be used to convert physical properties obtained from well logging data (e.g., mineralogy and pore structure) to elastic parameters (e.g., Young's Modulus and Poisson's Ratio) (Mavko et al., 2009). The reasonability of the model can significantly influence the accuracy of the calculated elastic parameters. A *BI* equation is capable of predicting brittleness using both the physical properties and the elastic parameters of the shale, but only when a suitable equation is applied.

Many studies have focused on discovering the intrinsic quality of brittleness, and many brittleness equations have been proposed by experts in the field. Based on Barnett shale samples, Rickman et al. (2008) found that a high Young's Modulus (*YM*) and a low Poisson's Ratio (*PR*) are indicators of high brittleness, so they proposed a brittleness index equation based on these parameters. Their discovery has been widely accepted in the industry, and a series of improved equations were built based on their proposal. Guo et al. (2012a) modified the equation by dividing *YM* by *PR*, justified by the idea that the *BI* is positively correlated with *YM* and negatively correlated with *PR*. Liu et al. (2015) improved upon Guo's equation by using normalized values for *YM* and *PR*.

In recent years, experts have proposed other elastic parameters to describe brittleness. Guo et al. (2012a, 2012b) proposed using the ratio between Lame's Coefficients (*LC*) to predict brittleness. Chen et al. (2014) found that the ratio between *YM* and *LC* can be used to identify brittle areas. Huang et al. (2015) derived a brittleness equation for tight reservoirs after comparing the sensitivities of different brittleness equations. Published equations have mostly focused on describing the sensitivities of different mathematical combinations of elastic parameters to brittleness, while largely have ignored the physical meanings of these elastic parameters. However, the brittleness of rock is also influenced by pore structure, mineralogy, and other physical properties. Analyzing the relationship between physical properties and brittleness-sensitive parameters is helpful for demonstrating the feasibility and sensitivity of different *BI* equations. A reasonable rock physics model can link two categories of parameters, so building a proper rock physics model seems both significant and straightforward.

In terms of rock physics modeling, the construction of shale rock physics models is still in its exploratory stage. Geophysicists have committed to building a reasonable rock physics model for shale, but its properties have proven complicated and difficult to be described using a single model. For example, before an anisotropic model can be constructed, we need to understand the origins of the shale's anisotropy and choose a reasonable set of theories to describe these origins. Shale usually exhibits strong vertical transverse isotropy (VTI), and the origins of shale anisotropy can be attributed to lamination, micro-fractures, and mineralogy. (1) Depositional lamination of clay and kerogen particles serves as a main contributing factor to VTI properties (Johansen et al., 2004; Vernik et al., 1992, 1997). (2) Scanning Electron Microscopy (SEM) images indicate an abundance of irregular pores and horizontal micro-fractures in shale, which can also enhance its anisotropy (Sayers, 1994). (3) Clay minerals are diverse and include kaolinite, chlorite, and illite, which can result in intrinsic anisotropy of clay minerals (Sayers, 2005; Guo et al., 2015). Clay mineral modeling is a significant foundation for shale model construction. Meanwhile, the properties of kerogen present another issue that cannot be ignored (Vanario et al., 2008);. Kerogen modeling is one of the difficulties in shale modeling because of its special physical properties (very low bulk modulus and shear modulus).

Vernik and Nur (1992) attempted to model a laminated clay and kerogen mixture based on its Backus average (Backus, 1962), which yielded a good prediction except for C_{33}. Vernik and Landis (1996) identified the source of this predicted error as the lamination of clay/kerogen and introduced an empirical parameter to correct the problem. Sayers et al. (2013) raised concerns that the Backus average is not sufficient to model kerogen in shale since the empirical fitting index seems to have no physical meaning. In addition, Guo et al. (2013) claimed that the Backus average could only perform well when the mineralogy of the shale is simple. Zhu et al. (2012) treated kerogen as a solid substitution based on the Brown-Korringa theory (Brown and Korringa, 1975), and they divided the pore space into solid and fluid pore spaces. Bandyopadhyay (2009) and Wu et al. (2012) simulated kerogen-rich shale based on an anisotropic differential effective medium (DEM) approach, and they found that when they treated kerogen as the matrix material, they obtained better predictions of C_{33} than did Vernik (1996). However, DEM has the drawback of requiring a background material and a set order for the other minerals. Varying this order can introduce

theoretical error, and while setting kerogen as the background can result in better predictions, the reality is that it is usually embedded in a clay background (Figure 1). Sayers (2013) claimed that this disagreement between theoretical modeling and ground truth may result from the disconnection between clay and kerogen.

Our study aimed to address the problems described above. We started by constructing a shale rock physics model based on an anisotropic self-consistent approximation (SCA) and a DEM theory to model kerogen in shale. SCA+DEM allowed us to build an intercoupled clay-kerogen block (CKB), which may solve the disconnection issues identified by Sayers (2013). The feasibility of this model was proved by comparing it with other models. In addition, sensitivity analysis of different elastic parameters was conducted for anisotropic conditions, and the model linked the physical parameters with the sensitive parameters of brittleness.

Rock physics model for kerogen-rich shale

Model construction

Based on anisotropic SCA+DEM theory (Hornby et al., 1994), we simulate the kerogen in shale by constructing mutually coupled clay kerogen blocks and obtain SEM images. The SEM images present detailed information of shale in underground reservoirs. The detailed features will provide valuable information for the construction of reasonable rock physical models. Figure 1 are SEM images that show a shale formation from X well in Southwest China. It is from the geological report of our target formation and shows the typical character of kerogen-rich shale. These images show bright white dots corresponding to brittle minerals (quartz or calcite), and light- and dark-brown background minerals corresponding to clay and kerogen, respectively, which are both ductile minerals. Based on the geochemical test report, this shale is mainly composed of quartz and feldspar, and the matrix is primarily clay and kerogen. The structural forms of brittle and ductile minerals are typically quite different. Ductile minerals (clay and kerogen) are usually formed from laminated deposition, while brittle minerals (quartz, calcite, and feldspar) are separately embedded in this laminated background. Hence, in our model, we first dealt with clay and kerogen by building a laminated clay-kerogen background, and then we added other brittle minerals into this background. As mentioned above, clay and kerogen are fine-grained sediments that form the matrix of the shale, and they intercouple with each other quite well. So, the first step to construct a model was to select a proper effective theory to simulate this intercoupled clay-kerogen background with its laminated form.

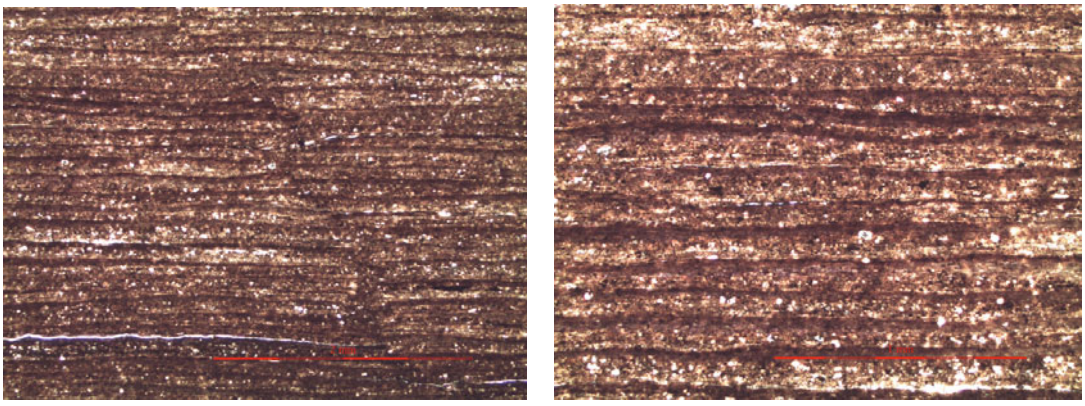

(a) Scanning scale: 2 mm (b) Scanning scale: 1 mm

Fig.1 SEM images of shale formation from X well, Southwest China.

As mentioned above, kerogen has unique physical and elastic properties. For instance, the bulk and shear moduli of kerogen are as low as 2.9 GPa and 2.7 GPa, respectively, while those of quartz are 37 GPa and 44 GPa, respectively. Meanwhile, the density of kerogen is relatively low, which causes kerogen-rich shale formations to have comparatively low densities. As a result, kerogen behaves more like a fluid rather than a mineral, and traditional theories that are used to model mineral skeletons are not able to model a kerogen-rich background.

The n-phase SCA method (Berryman, 1980, 1995) is popular in shale modeling since it can model all mineral phases and the fluid phase simultaneously. However,

many studies have shown that for a mixture of fluid and solid, the elastic modulus predicted by SCA often coincides with the upper bound of the Hashin-Shtrikman (HS) bound (Hashin and Shtrikman, 1963) at porosities below 40% (Hornby et al., 1994; Das and Batzle, 2009), which means that the softer fluid phase in the rock is surrounded by the harder mineral phase, and the pore fluid is isolated in this scenario.

The HS bound can be used to test the feasibility of SCA. If the detailed mineral arrangement of the rock is unknown, the HS bound can provide a reasonable prediction range (Mavko et al., 2009). Assuming two mineral phases, one softer and the other stiffer, the lower bound indicates the scenario in which the stiffer mineral is surrounded by the softer mineral, and the upeer bound indicates the opposite. If the prediction falls between these bounds, the two phases are intercoupled.

Bulk and shear modulus predictions made by SCA are shown in Figure 2. The bulk and shear modulus values for clay were 25 GPa and 9 GPa, respectively, and kerogen's elastic modulus values were as defined above. The SCA predictions reached the lower HS bound around 80%, which means the bi-connected range for the clay-kerogen mixture is around 20–80%. Since the shear modulus of kerogen is not zero, the bi-connected range for this mixture is wider than that of fluid-saturated rock (40–60%). However, the volume fraction of kerogen is still unlikely to reach that range in real reservoirs, which means SCA is insufficient to model kerogen in shale on its own.

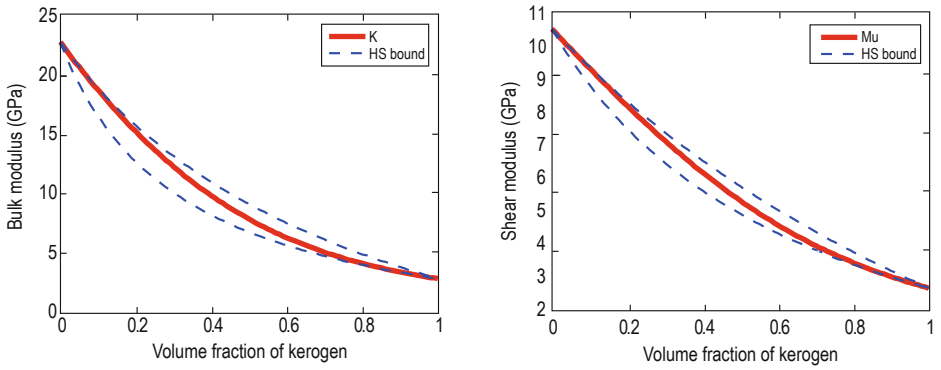

(a) Bulk modulus (b) Shear modulus

Fig.2 Predictions of effective bulk and shear moduli based on SCA as kerogen concentration varies.
The red line indicates the effective result of SCA, and the blue dashed lines indicate the upper and lower boundaries of HS.

To address this limitation, we modeled the clay-kerogen mixture based on SCA+DEM theory. Different from SCA theory (Berryman, 1980), this combined approach is able to keep the mineral phase (clay) and fluid phase (pore fluid) connected with each other. We treated kerogen as a fluid for the purposes of SCA+DEM. This model doesn't require the selection of a background mineral, so we avoided that weakness of the DEM approach as well. Sayers (2013) proposed that the prediction errors of C_{33} in Vernik (1996) were caused by ignoring the connectivity between clay and kerogen. Hence, SCA+DEM can hopefully solve this issue at the same time.

After building an intercoupled CKB, we modeled a typical lamination similar to the striation in Figure 1. Bond transforms and Voigt-Reuss-Hill (VRH) averages were performed in our modeling. Bond transforms helped us model different types of CKBs with different deviation angles. As shown in Figures 3a and 3b, variations of the angle caused the properties of the CKB to vary, even from VTI to HTI. The physical meaning of the deviation angle is the dip angle of the formation. A dip angle of zero indicates that all clay and kerogen are perfectly laminated; however, real shale formations never exhibit perfect lamination due to tectonic transfer (Hornby et al., 1994). Thus, based on the CKBs that we calculated by Bond transform, we introduced VRH theory to combine several identical CKBs with different dip angles and we simulated their effective properties. Each CKB had a unique deflection angle, θ, with a Gaussian distribution (Figure 3c). The mean value of this distribution was zero, which indicates that the majority of CKBs were laminated to represent VTI properties. The extent of lamination was controlled by the variance, i.e., low variance means the majority of the deflection angles are near zero, and therefore shows the strongest lamination. Based on empirical observations from the SEM images, we set the variance 20 (this would vary according to the extent of lamination for other real formations).

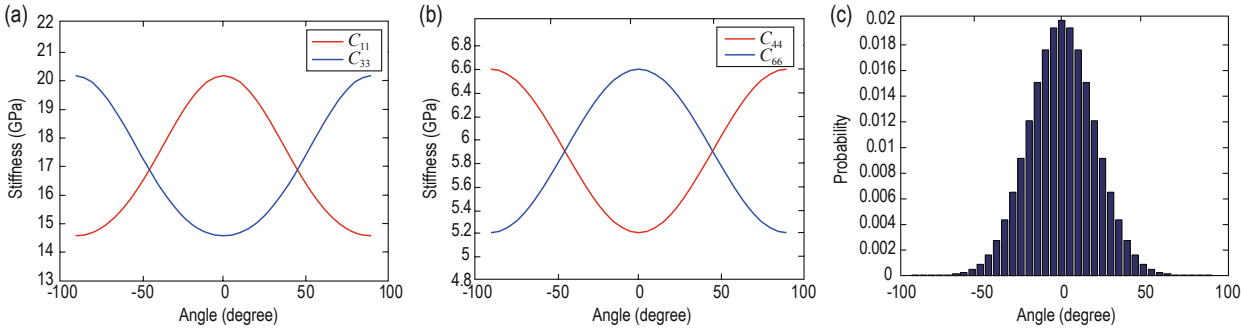

Fig.3 Dependence of the CKB on deflection angle.

(a) C_{11} (red line) and C_{33} (blue line) and (b) C_{44} (red line) and C_{66} (blue line); (c) Histogram of angles showing a normal distribution that is satisfied by many CKBs.

After constructing the ductile VTI background, the next step was to simulate the discrete brittle minerals (quartz, feldspar, etc.) within it. All kinds of brittle minerals were mixed using the VRH average, and an anisotropic DEM was proposed to add the brittle mixture into the ductile background. DEM makes a high-frequency assumption such that its inclusion phase is discrete, which makes it suitable for brittle minerals that are usually isolated.

Rock with complicated mineralogy (like shale) usually develops a range of pore types (Ba et al., 2008, 2011; Huang et al., 2015). For instance, inter-particle pores, organic pores, and micro-fractures usually exist in clay and kerogen. Our target formation was over-mature, which means the majority of micro-fractures were cemented or compacted, so we did not consider micro-fractures in our model. Meanwhile, the low porosity and permeability of shale usually result from the separate distribution of clay-related pores. Hence, we assumed that clay-related pores were isolated and we used anisotropic DEM to model them.

Based on the criteria described above, we built our kerogen-rich shale model as follows (Figure 4):

(1) Anisotropic SCA+DEM was performed to build the intercoupled CKBs.

(2) The lamination of each CKB was modeled by rotating and combining many identical CKBs. The properties of these rotated CKBs were calculated based on Bond transforms, and VRH averages were used to simulate the effective combination medium.

(3) Brittle minerals were mixed by VRH averages.

(4) The brittle mixtures and pores were added into the clay-kerogen backgrounds to obtain our final effective results. The pore fluid mixture was calculated by the Wood equation.

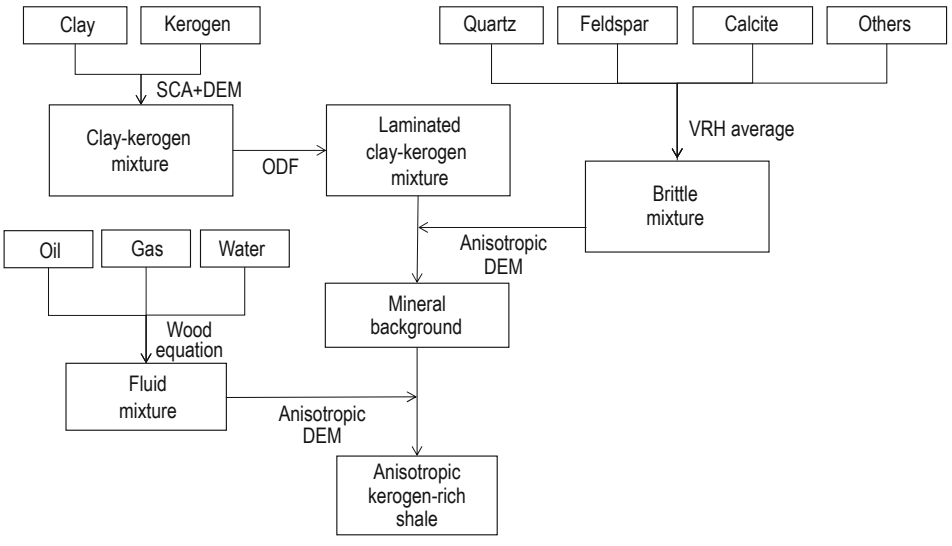

Fig.4 Workflow of kerogen-rich rock physics modeling.

Model test and theoretical analysis

In order to test the feasibility and accuracy of our model, especially its capacity to model kerogen in shale, we compared the predictions of the SCA+DEM model with other theoretical results (e.g., Backus average, DEM, etc.). We then selected a real shale sample from the Bazhenov formation and predicted its effective properties using our model.

(a) Feasibility of SCA+DEM

Figure 5 shows theoretical results of SCA+DEM and three other models as compared with real data. The elastic parameters of pure kerogen and pure shale are shown in Table 1, which were derived by Sayers (2013) and based on shale samples quoted from Vernik and Landis (1996).

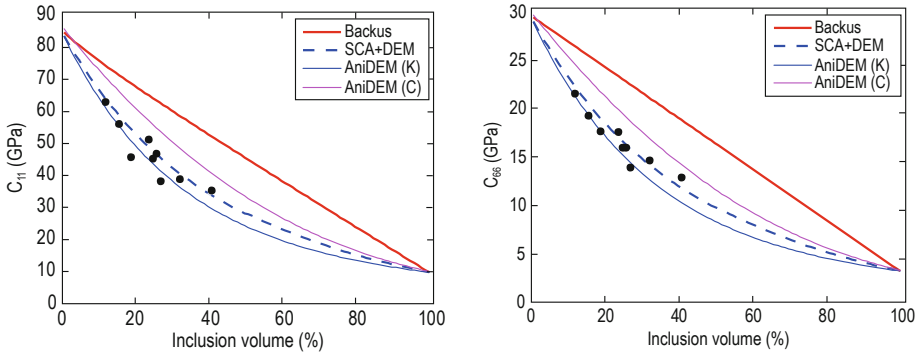

Fig.5 Theoretical predictions of elastic parameters based on different models with different kerogen inclusion. The abscissa is the volume fraction of kerogen, and the ordinate is the elastic tensor, either C_{11} (a) or C_{66} (b). The red lines represent the predictions of the Backus average, the pink lines represent the predictions of an anisotropic DEM with a shale background, the solid blue lines represent the predictions of an anisotropic DEM with a kerogen background, and the dashed blue lines represent the predictions of our SCA+DEM method. The black dots are data points from Bakken shale, quoted from Vernik and Liu (1997).

Table 1 Properties of kerogen and shale quoted from Sayers (2013)

Component	Density (g/cc)	C_{11} (GPa)	C_{33} (GPa)	C_{44} (GPa)	C_{66} (GPa)	C_{13} (GPa)
Kerogen	1.25	9.8	9.8	3.2	3.2	3.4
Shale	2.73	85.6	65.5	24.6	29.7	21.1

From Figure 5, we see that the traditional Backus average overestimates the data, as Vernik et al. (1996) and Sayers (2013) have found. The DEM models are better, but they overestimate the values when the kerogen is included in shale and underestimate them when shale is included in a kerogen background. The best fit comes from the dashed blue lines calculated by using the SCA+DEM theory. From this, we concluded that the feasibility of the SCA+DEM approach is verified.

(b) Feasibility of rock physics model

Based on our constructed model, we predicted values for a real core sample that were published by Vernik and Landis (1996), which is shown in Table 2. And the properties of individual mineral were quoted from Mavko et al. (2009). The data were also used by Wu et al. (2012) to test their model.

Table 2 Volume percentage and elastic moduli for each ingredient of the Bazhenov shale

	Quartz/Feldspar	Carbonate	Clay	Pyrite	Kerogen	Porosity	Fluid (brine)
% Vol.	46	3	48	3	16.8	4.12	N/A
K (GPa)	37	76.8	22.9	147.4	2.9	N/A	2.2
μ (GPa)	44	32	10.6	132.5	2.7	N/A	0

The stiffness of the CKBs that were predicted using SCA+DEM were C_{11} = 20.18 GPa, C_{33} = 14.57 GPa, C_{44} = 5.20 GPa, C_{66} = 6.60 GPa, and C_{13} = 5.99 GPa. Many identical CKBs were rotated based on the distribution

function (Figure 3c). Mean values and variances of the Gaussian distribution were equal to zero degree and 20 respectively, which represent the lamination of shale. The stiffness of the brittle mineral composite was calculated by VRH, where K = 39.9 GPa and μ = 42.4 GPa. DEM was performed to add the brittle mixture into the ductile background. Finally, the anisotropic DEM was used to add the brittle mixture into the effective mixture with an aspect ratio of 0.3.

Table 3 shows that our model (in bold) closely matches the real data and is better suited to estimate the stiffness of the Bazhenov samples than the other models. The SCA+DEM method yielded the minimum relative error, which proves the feasibility and capability of our model.

Table 3 Empirical measurements and predictions of stiffness of a shale field sample based on different models, with error analysis. The shale sample was from the Bazhenov formation as quoted from Vernik et al. (1997)

	C_{11} (GPa)	C_{33} (GPa)	C_{44} (GPa)	C_{66} (GPa)	Error
Real measured values by Vernik et al. (1997)	42.38	26.23	8.68	15.23	0
Wu et al. (2012)	45.45	31.33	6.87	17.62	0.0089
Our result (SCA+DEM)	**40.93**	**24.48**	**10.07**	**15.75**	**0.0017**
Result (Backus average)	42.00	22.33	9.81	16.13	0.0115
Result (DEM with shale background)	41.23	22.92	9.68	15.88	0.0068
Result (DEM with kerogen background)	42.19	23.8	10.0	16.14	0.0054

Analysis of brittleness index equation

In this section, the sensitivity and characteristics of different classical *BI* equations are analyzed based on our constructed model in terms of anisotropy.

Classical brittleness index equations

As mentioned above, the most commonly used brittleness equations can be divided into two categories: weight content methods (WCMs), which represent the brittleness of rock by using the volume percentage of brittle minerals, and elastic parameter methods (EPMs), which describe the brittleness of rock based on elastic parameters such as *YM*, *PR*, and *LC*. In addition, we subdivided EPMs into *YM*/*PR*-based equations and Lame's Coefficient equations according to their different types of elastic parameters. According to equations (1)–(9), *BI*_1 through *BI*_3 and *BI*_6 through *BI*_8 are EPMs, while *BI*_4 and *BI*_5 are WCMs. In addition, *BI*_1 through *BI*_3 are *YM*/*PR*-based brittleness index equations.

Rickman et al. (2008) proposed an average brittleness equation based on their analysis of the Barnett shale given by

$$\Delta YM = \frac{YM - 1}{8 - 1}, \quad \Delta PR = \frac{0.4 - PR}{0.4 - 0.15},$$

$$BI = \frac{\Delta YM + \Delta PR}{2} \times 100, \tag{1}$$

Since the *YM* and *PR* of shale samples from the Barnett shale fall mainly in the ranges 1–8 and 0.15–0.4, respectively, ΔYM and ΔPR were proposed as the normalized Young's Modulus and normalized Poisson's Ratio, respectively.

The standard definitions of Rickman's equations are

$$YM_{norm} = \frac{100(YM - YM_{min})}{(YM_{max} - YM_{min})},$$

$$PR_{norm} = \frac{100(PR - PR_{max})}{(PR_{min} - PR_{max})},$$

$$BI\_1 = \frac{YM_{norm} + PR_{norm}}{2}. \tag{2}$$

where YM_{norm} and PR_{norm} are the normalized terms, which correspond to ΔYM and ΔPR in equation (1).

Guo et al. (2012) constructed their *BI* as

$$BI\_2 = \frac{YM}{PR}. \tag{3}$$

Liu et al. (2015) defined the *BI* by the ratio of the normalized *YM* to the normalized *PR* as

$$BI\_3 = \frac{YM_{norm}}{PR_{norm}}. \tag{4}$$

*BI*_4 and *BI*_5 are WCM-based brittleness index equations given by

$$BI\_4 = \frac{Quartz}{Total} * 100\%, \tag{5}$$

$$BI\_5 = \frac{1 - V_{sh}}{Total} * 100\%, \tag{6}$$

where *Quartz*, Total, and V_{sh} represent the weight contents of quartz, total minerals, and clay content, respectively.

Guo et al. (2012) defined the *BI* using *LC* as

$$BI\_6 = \frac{\lambda + 2\mu}{\lambda}. \tag{7}$$

Chen et al. (2014) indicated that the ratio of the *YM* and Lame's Coefficient can be used to represent a highly brittle formation as

$$BI\_7 = \frac{YM}{\lambda}. \tag{8}$$

Note that *BI*_6 through *BI*_8 are brittleness indexes based on LC.

Huang et al. (2015) proposed a *BI* that compares the sensitivity of different types of combinations of elastic parameters as

$$BI\_8 = \frac{3\kappa - 5\lambda}{\lambda} = \frac{2\mu - 2\lambda}{\lambda} = \frac{1}{\nu} - 4, \tag{9}$$

where κ is the bulk modulus.

Different *BI* equations have different areas of focus. As a result, we selected an appropriate equation while doing brittleness analysis of different types of formations. The suitability of each equation is described in Figure 6.

*BI*_1 through *BI*_3 all show that the brittleness index is proportional to *YM* and inversely proportional to *PR*. The weighted average in *BI*_1 treats *YM* and *PR* equally, and it doesn't consider the difference between *YM* and *PR* to be related to brittleness. This kind of rough average has no physical meaning and should be continuously improved and calibrated by more shale data.

*BI*_2 and *BI*_3 have similar forms, with both using the ratio between *YM* and *PR*. The only difference is that *BI*_2 uses actual values of *YM* and *PR* while *BI*_3 normalizes *YM* and *PR*. This normalization process can avoid abnormal predictions resulting from the different magnitudes of *YM* and *PR* and can enhance the stability of *BI*_3's predictions. However, it varies the magnitude of *YM* and *PR* toward the same level, which may reduce the sensitivity of *BI*_3's predictions. Meanwhile, the value of *PR* may drop to 0 after normalization, which may also yield abnormal values, so these equations must be handled with care.

*BI*_4 and *BI*_5 are WCMs. *BI*_4 treats quartz as the brittle mineral while *BI*_5 treats both quartz and calcite as brittle minerals. *BI*_4 and *BI*_5 are simple to use, requiring just the volume fractions of brittle minerals as inputs, which makes WCMs effective and widely used.

WCMs need to assume that the rock is isotropic and that the prediction contains no anisotropic information. While the elastic parameters in EPMs, such as *YM*, *PR*, and Lame's parameters, are based on the isotropic concept, they can still be analyzed in an anisotropic way (equation (10)). In addition, EPMs take the effect of pore shape and pore fluid into consideration while WCMs only consider the mineralogical effects, thus making them rougher by comparison.

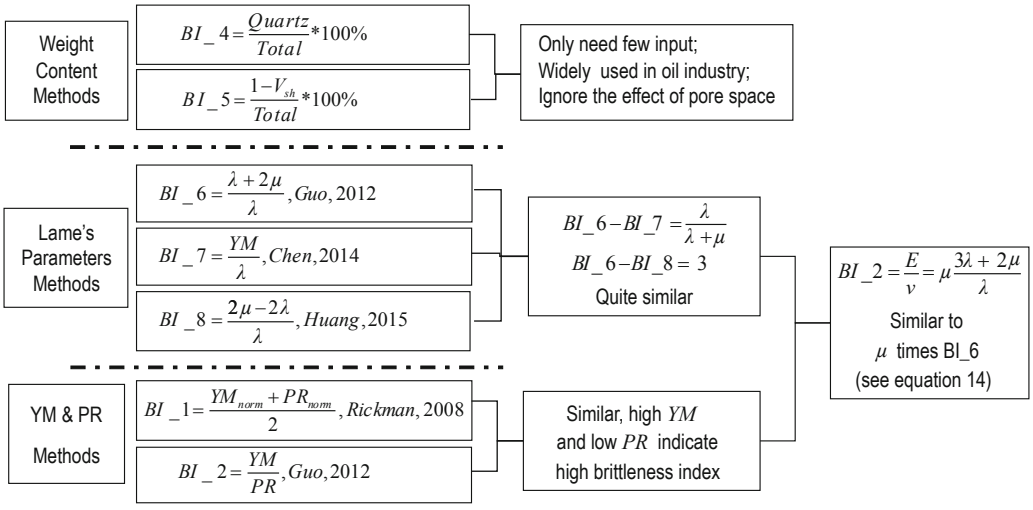

Fig.6 Definitions and comparison among different types of brittleness index equations.

Brittleness index sensitivities

In order to analyze the ability of a brittleness index equation to distinguish between different types of rock, the concept of a sensitivity index of brittleness (*BI*_sensitivity) has been introduced in recent papers (Huang et al., 2015). The brittleness values of silica-rich shale (volume fraction ratio of quartz:clay is 4:1) and clay-rich shale (ratio is 1:4) were calculated. The differences between these brittleness values were quantified, with a wide gap representing a high sensitivity.

This kind of sensitivity analysis relies on the other parameters being held constant. However, the brittleness of rock is usually a result of a combination of many parameters, which means that the sensitivities of different equations may vary as the physical properties of the rock vary. Hence, the sensitivities of *BI* equations must be discussed under the assumption of a specific physical condition. In order to analyze the effect of physical properties (e.g., mineralogy, pore fluid, and pore structure) on the sensitivity of *BI*, our study varied the mentioned physical properties based on our previously constructed model and quantitatively discovered the sensitivity values under different scenarios by introducing the sensitivity index.

Since our model is anisotropic, the sensitivity analysis was performed using a calculated elastic tensor,

$$C_{6*6}=\begin{bmatrix} \lambda_{\parallel}+2\mu_{\parallel} & \lambda_{\parallel} & \lambda_{\perp} & 0 & 0 & 0 \\ \lambda_{\parallel} & \lambda_{\parallel}+2\mu_{\parallel} & \lambda_{\perp} & 0 & 0 & 0 \\ \lambda_{\perp} & \lambda_{\perp} & \lambda_{\perp}+2\mu_{\perp} & 0 & 0 & 0 \\ 0 & 0 & 0 & \mu^{*} & 0 & 0 \\ 0 & 0 & 0 & 0 & \mu^{*} & 0 \\ 0 & 0 & 0 & 0 & 0 & \mu_{\parallel} \end{bmatrix}, \tag{10}$$

where $\lambda_{\parallel}$ and $\mu_{\parallel}$ represent the horizontal LC, $\lambda_{\perp}$ and $\mu_{\perp}$ represent the vertical LC, and μ^{*} is the shear modulus that is related to both vertical and horizontal directions (Sun, 2007).

Figure 7 shows the sensitivity analyses of the elastic moduli by varying the mineralogy. The ratio between quartz and clay volume content varied from 1:4 to 4:1, while the other physical parameters were unchanged (porosity was held at 10% and the volume fractions of kerogen and calcite were equal to 10% and 40%, respectively).

The sensitivity index equation for mineral variations is given by

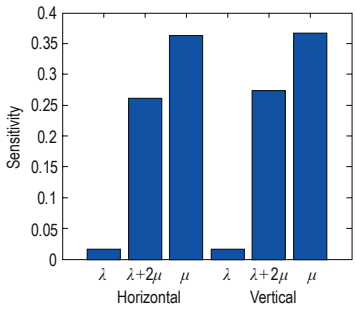

Fig.7 Sensitivity analyses of different elastic moduli by varying the mineral content.

$$SI_{\text{mineral}}=\left|\frac{C_{\text{quartz}}-C_{\text{clay}}}{C_{\text{quartz}}}\right|, \tag{11}$$

where *SI* is the sensitivity index, *C* represents the sensitive elastic parameters (e.g., λ, μ, and λ+2μ), and the subscripts indicate the silica- or clay-rich shale. Goodway et al. (2010) pointed out that highly brittle formations usually have low $\lambda\rho$ and medium $\mu\rho$. They also mentioned that λ is usually called the "fluid factor," which is sensitive to fluid variations, while μ often represents the shear capability of the skeleton and is therefore called the "lithology factor." Figure 7 reinforces these definitions where the lithology factor, μ, shows the highest sensitivity to varying lithologies, while the fluid factor, λ, has the lowest sensitivity.

In order to analyze the sensitivity by varying the other types of minerals, our study also scaled the volume fraction of calcite and kerogen. The prediction of the SI_{mineral} showed that the trend of the sensitivity was consistent, and the magnitude of SI_{mineral} varied according to the variations of the elastic moduli.

Figure 8 shows the sensitivity analyses of the elastic moduli by varying the pore fluid. The pore fluid varied from water-saturated to gas-saturated, while the other parameters were unchanged, i.e., the volume fractions of

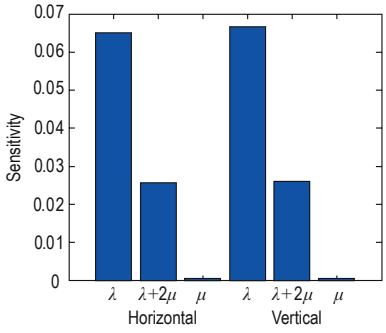

Fig.8 Sensitivity analyses of different elastic moduli by varying the pore fluid.

quartz, calcite, clay, and kerogen were set to 10%, 40%, 40%, and 10%, respectively, while the porosity was 10% and the pore aspect ratio was 1.

The sensitivity index for fluid variations is given by

$$SI_{\text{fluid}} = \left| \frac{C_{\text{water}} - C_{\text{gas}}}{C_{\text{water}}} \right|, \qquad (12)$$

where the subscripts indicate water-saturated or gas-saturated shale. In this situation, the sensitivity of the fluid factor, λ, is higher than that of the lithology factor, μ.

Figure 9 shows the sensitivity analyses of the elastic moduli when the pore structure of the shale was altered. The pore aspect ratio was varied from 1 to 0.1, while the other parameters were unchanged, i.e., the volume fractions of quartz, calcite, clay, and kerogen were 10%, 40%, 40% and 10%, respectively, while the porosity was held at 10% and the pore fluid was water.

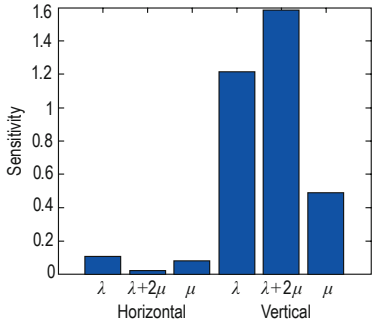

Fig.9 Sensitivity analyses of different elastic moduli by varying the pore shape.

The sensitivity index for pore shape variations is given by

$$SI_{\text{asp}} = \left| \frac{C_{\text{spherical}} - C_{\text{flat}}}{C_{\text{spherical}}} \right|, \qquad (13)$$

where the subscripts indicate pore aspect ratios equal to 1 (spherical) or 0.1 (flat). Figure 9 shows that the sensitivities of the elastic parameters in the vertical direction are vastly higher than those in the horizontal direction.

Figures 7–9 demonstrate that the sensitivities of our elastic parameters are related to mineralogy, pore fluid, and pore structure; thus, they will vary for different types of shale. In order to analyze the brittleness of different types of formations, we needed to take into consideration a range of physical effects rather than only analyzing the effect of mineralogy. For a formation with relatively high porosity and complicated pore fluid phases, it is better to choose a fluid-sensitive *BI* equation, while for target areas with low porosity and complicated lithology, a lithology-sensitive *BI* may yield better predictions.

*BI*_2 and *BI*_6 are based on *YM*/*PR* and *LC*, respectively. If λ has the same order of magnitude as μ, then *BI*_2 can be approximated as *BI*_6*μ. Since μ is the lithology factor, the *YM*/*PR*-based *BI*_2 is more sensitive to variations in lithology. Meanwhile, *BI*_6 through *BI*_8 are based on the form of *Vp*/*Vs*, which indicates that Lame's Coefficients-based equations are more sensitive to pore fluid variations, as described by

$$E = \mu \frac{3\lambda + 2\mu}{\lambda + \mu}, \quad \nu = \frac{\lambda}{2(\lambda + \mu)},$$

$$BI\_2 = \frac{E}{\nu} = \mu \frac{3\lambda + 2\mu}{\lambda}. \qquad (14)$$

Case study

The models and equations described above were used to predict the brittleness of the shale from a well located in Southwest China. Our target formation is part of the Longmaxi and Wufeng formations at a depth of 1900 to 2060 m at our well location.

Figure 10 displays a range of pertinent information related to this shale deposit, including logging data and predictions of brittleness based on different types of equations. The results of *BI*_1 and *BI*_2, which are both based on *YM* and *PR*, are similar to each other, which indicates the stability of this category of equations. *BI*_4 and *BI*_5, which are based on weight content, are not different to each other, which suggests that WCMs are rougher than EPMs. The predictions of WCMs rely too much on the accuracy of the mineral inversion procedure, and they usually result to lower precision. The predictions made by *BI*_6, *BI*_7, and *BI*_8, all of which are based on LCs, are very similar.

Although the EPMs based on *YM*/*PR* and LCs share some fundamental aspects, their overall prediction trends are quite dissimilar, especially at 2020 and 2060 m, which shows the different sensitivities of these two approaches.

One term in equation (14), $\frac{3\lambda + 2\mu}{\lambda}$, is quite similar to the definition for *BI*_6, $BI\_6 = \frac{\lambda + 2\mu}{\lambda}$, since λ and μ have the same order of magnitude. Hence, the predictions from *BI*_2 are similar to the product of μ and *BI*_6. Since μ is a lithology factor, *BI*_1 and *BI*_2

are more sensitive to variations of lithology than *BI*_6 through *BI*_8 (e.g., at 2020 m). By contrast, *BI*_6 through *BI*_8 are more sensitive to formations with higher porosity (e.g., at 2060 m).

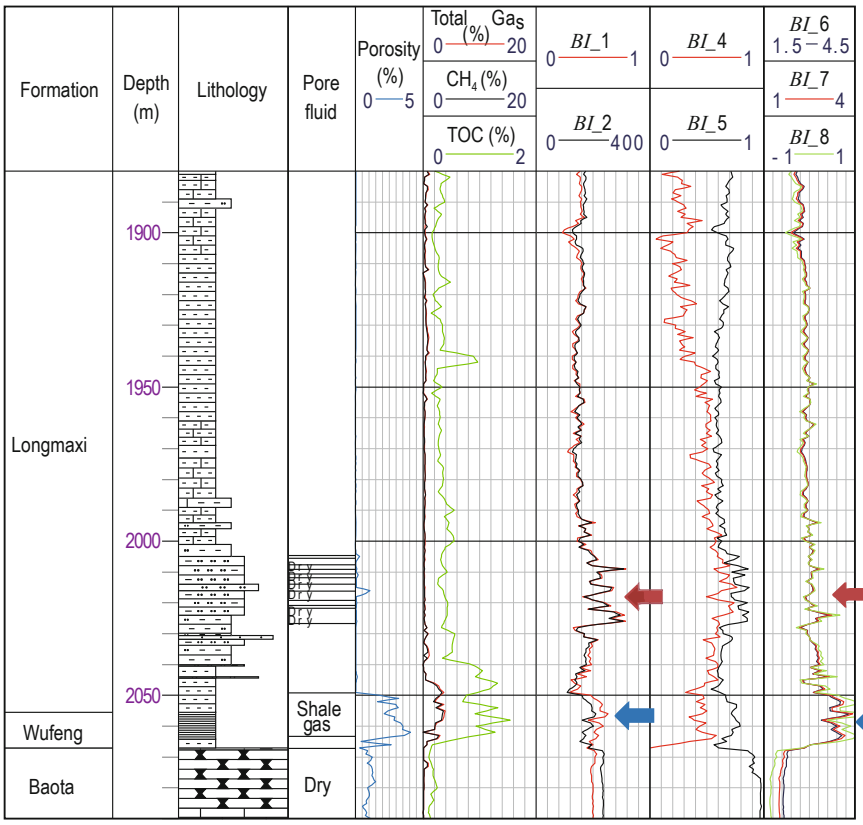

Fig.10 Observations and predictions of brittleness index from Well X.

The third through the sixth panels contain interpretations of empirical logging data. The seventh, eighth, and ninth panels show sets of predictions of brittleness, as grouped by equation type (*YM*/*PR* EPMs, weight-based WCMs, and *LC* EPMs, respectively). The red arrows and blue arrows highlight depths at which the EPMs behaved very differently from each other due to lithology and porosity, respectively.

In order to discover the inner relationship between these three types of methods, we built crossplots of *BI* and colored the data points using physical properties measured in the target Wufeng Formation.

Figure 11 shows a crossplot between two *YM*/*PR*-based equations, i.e., *BI*_1 (equation (2)) and *BI*_2 (equation (3)) proposed by Rickman et al. (2008) and Guo et al. (2012), respectively. The figure demonstrates that the two types of predictions coincide well with each other and that the brittleness of the rock is positively related to pore aspect ratio. As the pore aspect ratio increases, the elastic velocity of the rock increases, even as the density of rock stays constant. The increase in velocity can cause an increase in *LC*, and finally, result in an increase in *YM* and brittleness.

Figure 12 shows a crossplot between *BI*_2 and *BI*_6. Although the linear relationship is not as clear as in Figure 11, it still shows a generally positive relationship.

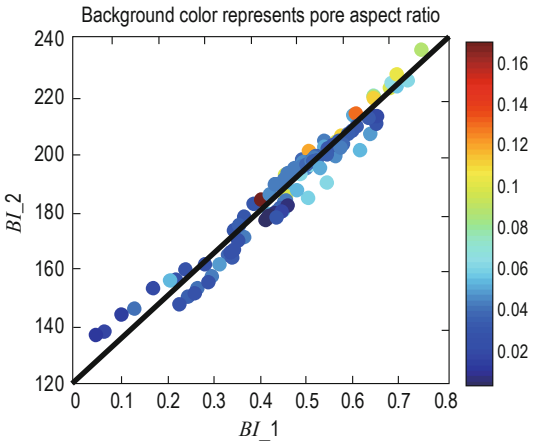

Fig.11 Crossplot of brittleness indexes *BI*_1 and *BI*_2.

The background color indicates the inverted pore aspect ratio, which represents the shape of the pore space (Qian et al., 2014).

When the pore aspect ratio is taken into consideration, the sensitivity of *BI*_6 clearly differs from that of *BI*_2 as the pore aspect ratio varies. *BI*_6 is more sensitive than *BI*_2, which means that it is able to better distinguish the brittleness of two data points. However, *BI*_2 has a higher sensitivity than *BI*_6 as the pore aspect ratio reaches high values.

Figure 13 shows a crossplot between *BI*_1 and *BI*_4. From the figure, it can be seen that *BI*_1 is much more sensitive than *BI*_4, which is based on the volume fraction of quartz. *BI*_4 cannot distinguish between different data points if the variations of the quartz content is minor, while *BI*_1 can clearly differentiate by aspect ratio. This is because *BI*_1 considers the effects of pore space, while *BI*_4 doesn't. This further reinforces our assertion that variations in pore structure can influence brittleness.

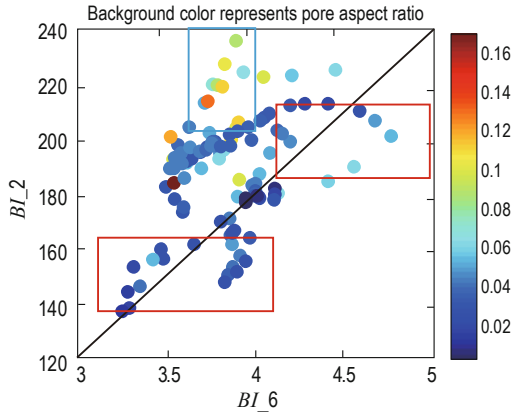

Fig.12 Crossplot of brittleness indexes *BI*_2 and *BI*_6. The background color indicates the inverted pore aspect ratio, which represents the shape of the pore space. The red rectangle indicates data points with relatively low pore aspect ratio while the blue rectangle indicates points with high pore aspect ratio.

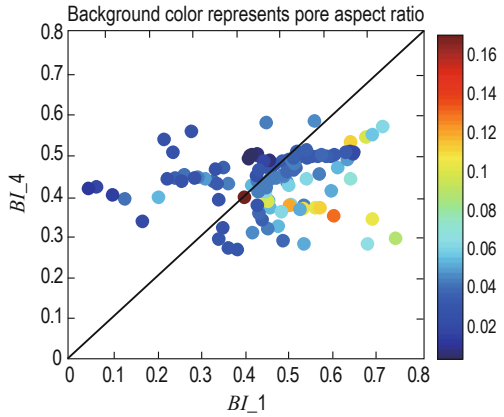

Fig.13 Crossplot of brittleness indexes *BI*_1 and *BI*_4. The background color indicates the inverted pore aspect ratio, which represents the shape of the pore space.

Analysis of rock physics templates

Brittleness index analysis based on our model

We built crossplots of brittleness based on our model, with the intent to discover the relationship between physical parameters and the *BI*.

Figure 14 shows the variations of *YM* and *PR* in terms of quartz content and porosity. Increases in porosity can cause an decrease of both *YM* and *PR*. However, increases in quartz content may increase the *YM* but

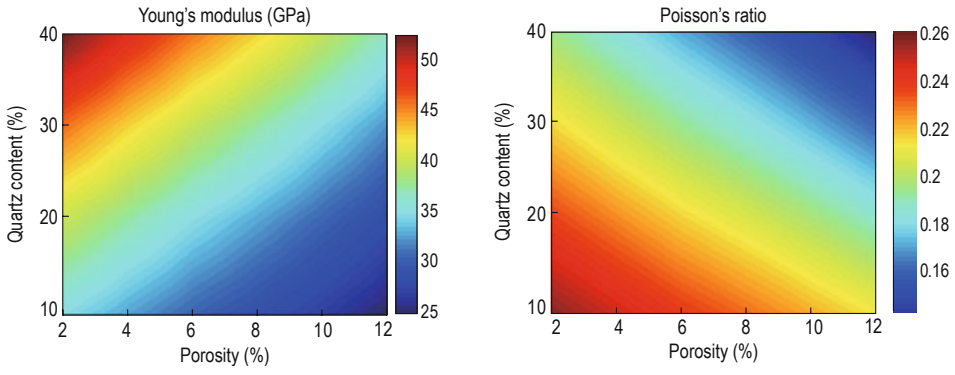

(a) *YM* (b) *PR*

Fig.14 Variations of (a) *YM* and (b) *PR* resulting from different porosity and quartz content, as indicated by the background color. The x-axis shows the variations of porosity from 2% to 12%, and the y-axis shows the variation of mineralogy with quartz content increasing from 10% to 40% and clay content dropping from 40% to 10%.

decrease the *PR*. In addition, *PR* is more sensitive to porosity than to mineralogy. Calcite and kerogen were held at 40% and 10%, respectively. The pore fluid was water, and the pore aspect ratio was set to 0.3, with mean value and variance of the normal distribution set to 0 and 20, respectively.

Figure 15 shows the variations of different types of brittleness indexes in terms of porosity and quartz content. The tendencies of *BI*_1 and *BI*_2 are similar, as are *BI*_6 through *BI*_8. *BI*_6 and *BI*_8 differ in magnitude by a value of 3, even though the trends are indistinguishable, which agrees with our previous discussion.

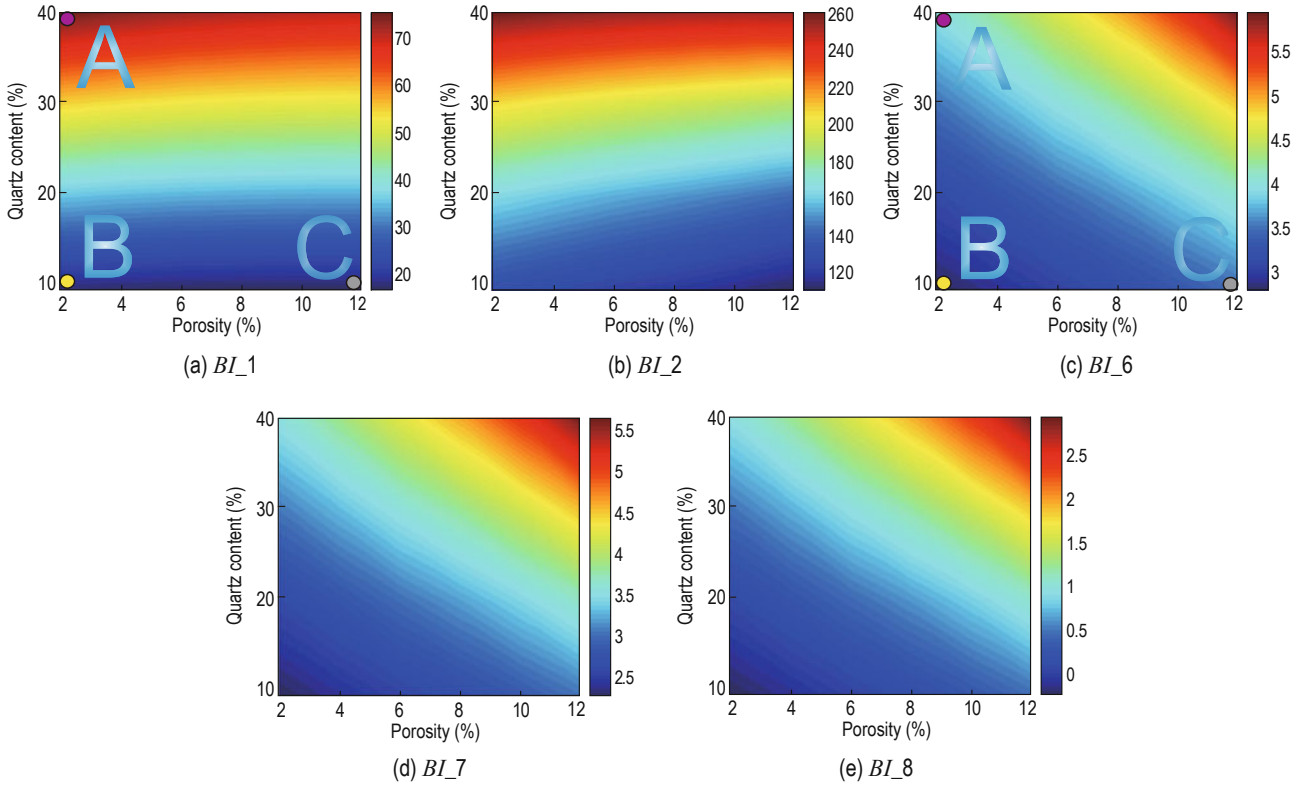

Fig.15 Variations of brittleness indexes from different porosity and quartz content. The purple point A represents a porosity of 2% and a quartz content of 40%, the yellow point B represents a porosity of 2% and a quartz content of 10%, and the gray point C represents a porosity of 12% and a quartz content of 10%.

In addition, as mentioned above, the differences between *BI*_1, *BI*_2, and *BI*_6 through *BI*_8 result from the term μ.

In order to analyze the sensitivity of the different brittleness indexes, we chose three representative points in Figures 15a and 15c. The three points represent three of the extreme combinations of porosity and quartz content. The predictions of these points based on Equations (2) and (7) are $BI\_1\_A = 75.99$, $BI\_1\_B = 18.12$, $BI\_1\_C = 17.37$, $BI\_6\_A = 4$, $BI\_6\_B = 2.823$, and $BI\_6\_C = 3.536$. Based on equations (11)–(13), we introduced a sensitive index to describe this sensitivity.

Points *A* and *B* both have relatively low porosity (2%) but with significantly different mineralogy, i.e., a quartz content from 40% to 10% and a clay content from 10% to 40%. Hence, we derived (15) to analyze the sensitivity of the *BI* to mineralogy as

$$SI_{BI} = \left| \frac{BI\_A - BI\_B}{BI\_A} \right|, \tag{15}$$

where *BI*_*A* and *BI*_*B* indicate the brittleness index at point *A* and point *B*, respectively, and SI_{BI} is the sensitivity index of brittleness. Note that a high value of SI_{BI} indicates high sensitivity.

SI_{BI}_1 and SI_{BI}_6 were calculated as 0.76 and 0.29, respectively. *BI*_1 is more sensitive to variations of mineralogy than *BI*_6, which means that *YM*/*PR*-based equations are more sensitive to mineralogy, confirming the results of our previous analysis.

Similarly, points *B* and *C* have similar mineral content (quartz content is 10% and clay content is 40%) but significantly different porosity, i.e., 2% to 12%, respectively. Hence, (16) can be used to describe the

sensitivity of the *BI* to porosity as

$$SI_{BI} = \left| \frac{BI\_B - BI\_C}{BI\_B} \right|, \quad (16)$$

where *BI_B* and *BI_C* indicate the brittleness index at point *B* and point *C*, respectively. SI_{BI}_1 and SI_{BI}_6 were found to be equal to 0.04 and 0.25, respectively, which means that *BI*_6 is more sensitive to porosity than *BI*_1.

Analysis of seismic attributes based on our model

The final application of this model is to decipher the relationship between seismic attributes and *BI*. Figure 16 is a set of crossplots four brittleness indexes *BI*_1, *BI*_2, *BI*_4, and *BI*_6. Porosity ranged from 2% to 12%, clay content ranged from 10% to 40%, pore fluid was a mixture of gas, oil, and water with volume ratios of 0.1:0.1:0.8, and the pore aspect ratio was 0.3. Based on this figure, the elasticity-based brittleness indexes (*BI*_1, *BI*_2, and *BI*_6) were all affected by porosity, while the Lame's Coefficients-based indexes were more sensitive to pore fluid. The mineralogy-based brittleness index *BI*_4 had no relationship with porosity, which is a critical drawback.

The porosity of a shale reservoir is usually higher than its surroundings. Hence, the sensitivity analysis in a high-porosity formation seems significant. Based on Figure 16d, when considering the mineralogical and porosity effects simultaneously, it is better to choose a zone with medium *YM* and low *PR*, instead of a zone with high *YM* and low *PR*.

In summary, brittleness predictions differed between the *BI* equations, which indicates that mechanical parameters are not only related to the mineralogy but also to the physical characteristics of the rock. A medium *YM* value and a low *PR* value indicate high brittleness with high porosity, which may be a potential area for shale exploration. These results match those of previous

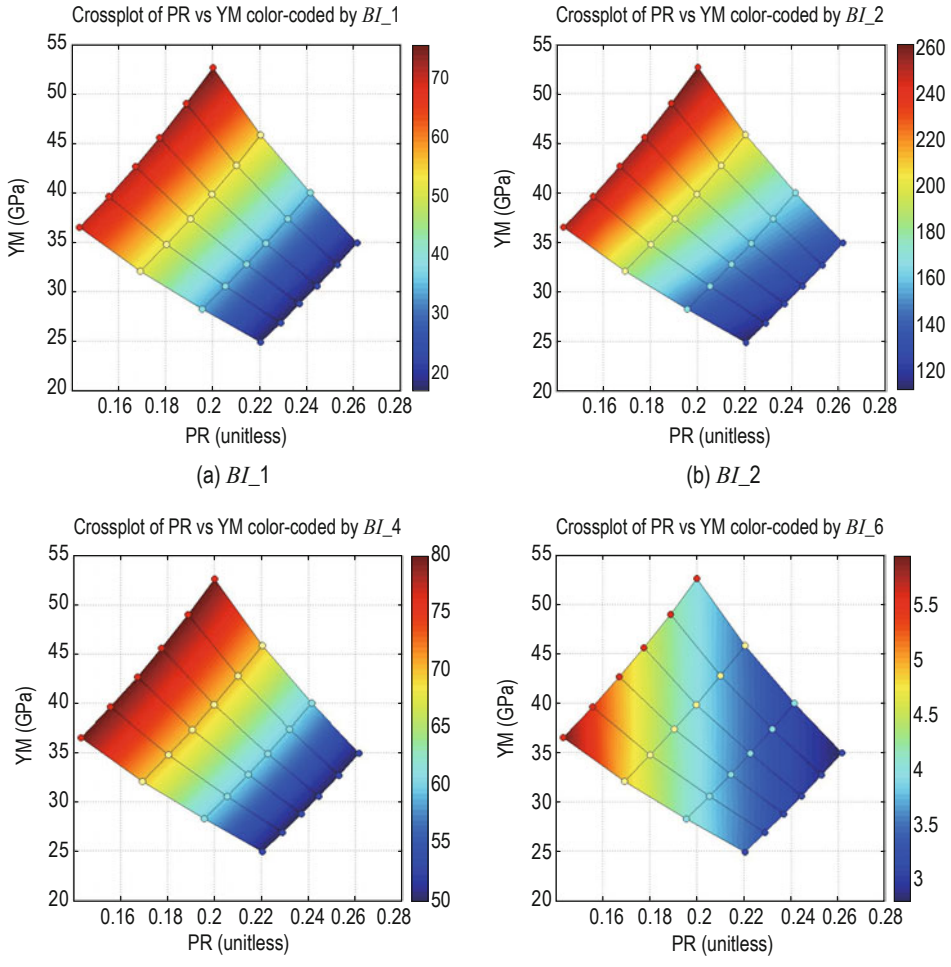

Fig.16 Crossplot of *YM* and *PR* for different brittleness indexes.

work (Huang et al., 2015).

Figure 17 shows crossplots between *Ip* and *Vp*/*Vs* together with empirical results from our target well. Our templates can cover the majority of data points, which demonstrates the practical utility of our model.

The tendencies of *BI*_1 and *BI*_6 vary significantly, which indicates that the sensitivities of these brittleness indexes vary with the physical properties of the shale. As porosity increases from 2% to 12%, the sensitivity of *BI*_1 to lithology was largely static, while *BI*_6 showed far greater sensitivity to lithology in the high-porosity range than the low-porosity range. As clay content increases from 10% to 40%, *BI*_1 becomes more sensitive to lithology than *BI*_6 in the low-porosity range, which proves that YM-based equations are more sensitive to lithology, while Lame's Coefficients-based equations are more sensitive to porosity/pore fluid.

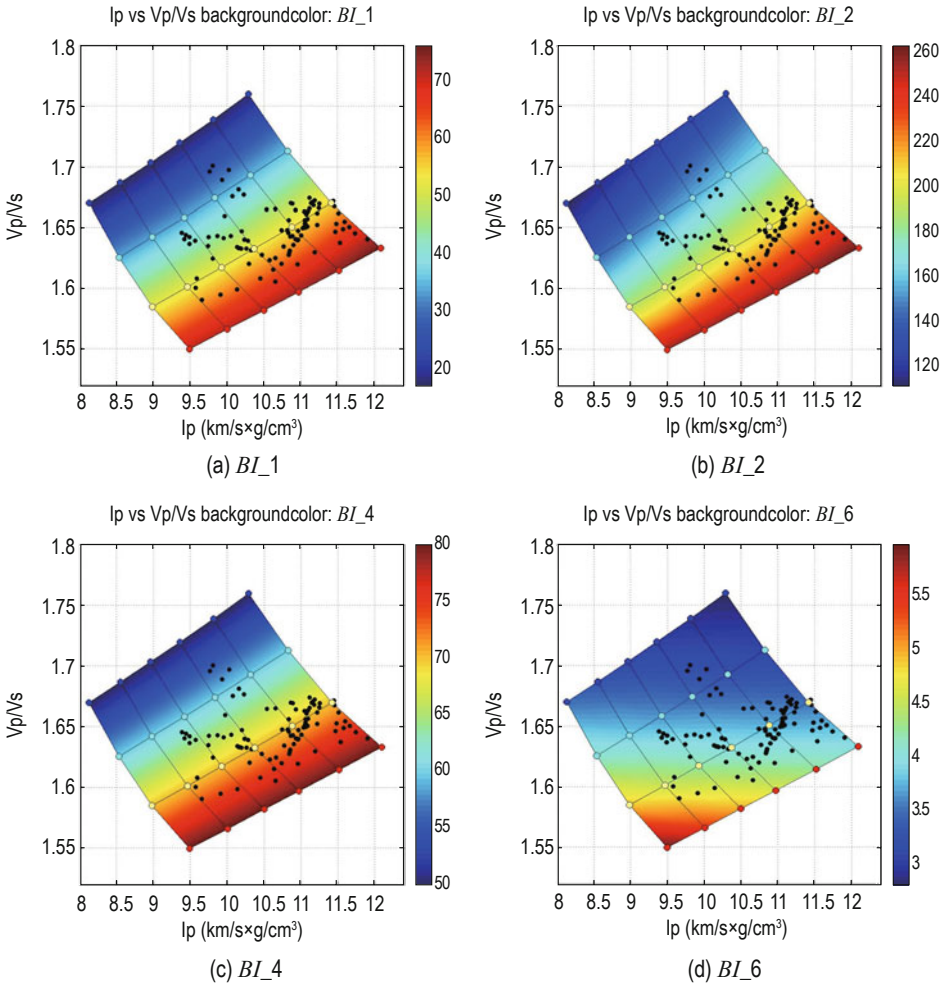

Fig.17 Crossplots of Ip and Vp/Vs for different brittleness indexes.
The black dots are from the target formation, which were calculated based on well logging data.

Conclusions

This study utilized a seismic rock physics model to analyze the brittleness of a kerogen-rich shale formation. By building crossplots of seismic attributes in terms of *BI*, we accurately predicted the *BI* of a shale deposit in Southwest China. The main conclusions of the study are the following.

(1) An anisotropic rock physics model was constructed for kerogen-rich shale formations. The SCA+DEM approach used by our model avoided the major drawbacks of traditional methods. SCA+DEM can be used to model intercoupled clay and kerogen mixtures that can improve the accuracy of shale modeling.

(2) Based on sensitivity analysis of brittleness, the predictions of EPMs are more accurate than WCMS and were related to the physical properties of the rock

(e.g., lithology, pore fluid, and pore structure). These properties were inherited by the brittleness indexes based on EPMs. *YM*-based brittleness indexes are more sensitive to variations in lithology, while Lame's Coefficients-based brittleness indexes are more sensitive to variations in pore fluid. Therefore, models need to account for the physical properties of formations when predicting brittleness.

(3) Results of crossplot from our model demonstrated the following: (i) an increase in clay content may cause the sensitivity of *Vp*/*Vs* to porosity to decrease; and (ii) as clay content increases, *YM* decreases and *PR* increases. However, as porosity increases, the sensitivity of *YM* to lithology gradually decreases and *PR* remains largely unaffected. This phenomenon indicates that *PR* is more reliable at distinguishing lithology than *YM* under high-porosity conditions. Low *PR* and medium *YM* indicate a brittle shale formation with relatively high porosity, which may indicate a "sweet spot" for shale exploration.

References

Bandyopadhyay, K., 2009, Seismic anisotropy: Geological causes and its implications to reservoir geophysics: PhD Thesis, Stanford University.

Ba, J., Carcione, J. M., and Nie, J. X., 2011, Biot-Rayleigh theory of wave propagation in double-porosity media: Journal of Geophysical Research Solid Earth, **116**(B6), B06202.

Ba, J., Cao, H., Yao, F. C., Nie, J. X., and Yang, H. Z., 2008, Double-porosity rock model and squirt flow in the laboratory frequency band: Applied Geophysics, **5**(4), 261−276.

Backus, G. E., 1962, Long-wave elastic anisotropy produced by horizontal layering: Jounal of Geophysical Research, **67**(11), 4427−4440.

Brown, R., and Korringa, J., 1975, On the dependence of the elastic properties of a porous rock on the compressibility of the pore fluid: Geophysics, **40**(4), 608−616.

Chen, J. J., Zhang, G. Z., Chen H. Z., and Yin, X. Y., 2014, The Construction of Shale Rock Physics Effective Model and Prediction of Rock Brittleness: 84th Annual International Meeting, SEG, Expanded Abstracts, 2861−2865.

Goodway, B., Perez, M., and Varsek, J., 2010, Seismic petrophysics and isotropic-anisotropic AVO methods for unconventional gas exploration: Leading Edge, **29**(12), 1500−1508.

Goodway, B., Chen, T., and Downton, J., 1999, Improved AVO fluid detection and lithology discrimination using Lamé petrophysical parameters; "λρ","μρ", &"λ/μ fluid stack", from P and S inversions: 69th Annual International Meeting, SEG, Expanded Abstracts, **16**(1), 2067.

Guo, Z., and Li, X. Y., 2015, Rock physics model-based prediction of shear wave velocity in the Barnett Shale formation: Journal of Geophysics & Engineering, **12**(3).

Guo, Z., Chapman, M., and Li, X. Y., 2012a, A shale rock physics model and its application in the prediction of brittleness index, mineralogy, and porosity of the Barnet Shale: 82th Annual International Meeting, SEG, Expanded Abstracts, 1−5.

Guo, Z., Chapman, M., and Li, X. Y., 2012b, Exploring the effect of fractures and microstructure on brittleness index in the Barnett Shale: 82th Annual International Meeting, SEG, Expanded Abstracts, 1−5.

Hashin, Z., and Shtrikman, S., 1963, A variational approach to the elastic behavior of multiphase materials: Mech Phys Solids, **11**, 127−140.

Hornby, B., Schwartz, L., and Hundson, J., 1994, Anisotropic effective-medium modeling of the elastic properties of shales: Geophysics, **59**, 1570−83.

Huang, X. R., Huang, J. P., Li, Z. C., et al., 2015, Brittleness index and seismic rock physics model for anisotropic tight-oil sandstone reservoirs: Applied Geophysics, **12**(1), 11−22.

Johansen, T. A., Ruud, B. O., and Jakobsen, M., 2004, Effect of grain scale alignment on seismic anisotropy and reflectivity of shales: Geophysical Prospecting, **52**(2), 133−149.

Qian, K., Zhang, F., Li, X. Y., et al., 2014, A Rock Physics Model for Estimating Elastic Properties of Organic Shales: 76th EAGE Conference & Exhibition Extended Abstract. Th D203 03.

Liu, Z. and Sun, Z., 2015, New brittleness index Brittleness Indexes and their application in shale/clay gas reservoir prediction: Petroleum Exploration and Development(in Chinese), 117−124.

Mavko, G., Mukerji, T., and Dvorkin, J., 2009, The rock physics handbook: Tools for seismic analysis of porous media. Cambridge University Press, England.

Rickman, R., Mullen, M. J., Petre, J. E., et al., 2008, A practical use of shale petrophysics for stimulation design optimization: All shale plays are not clones of the Barnett Shale: Annual Technical Conference and Exhibition. Society of Petroleum Engineers, SPE 115258.

Sayers, C. M., 1994, The elastic anisotropy of shales: Journal of Geophysical Research Atmospheres, **99**, 767-774.

Sayers, C. M., 2005, Seismic anisotropy of shales:

Geophysical Prospecting, **53**(5), 667−676.
Sayers, C. M., 2013, The effect of kerogen on the elastic anisotropy of organic-rich shales: Geophysics., **78**(78), 65−74.
Sun, C. Y., 2007, Theory and Methods of seismic Waves. China University of Petroleum of Press, Dong Ying.
Sondergeld, C. H., and Rai, C. S., 2011, Elastic anisotropy of shales: The Leading Edge., **30**(3), 324−331.
Vanorio, T., Mukerji, T., and Mavko, G., 2008, Emerging methodologies to characterize the rock physics properties of organic-rich shales: The Leading Edge: **27**(6), 780−787.
Vernik, L., and Nur, A., 1992, Petrophysical analysis of the Cajon Pass Scientific Well: Implications for fluid flow and seismic studies in the continental crust: Journal of Geophysical Research Atmospheres, **97**(B4), 5121−5134.
Vernik, L., and Liu, X., 1997, Velocity anisotropy in shales: A petrophysical study. Geophysics, **62**(2), 521−532.
Vernik, L., and Landis, C., 1996, Elastic anisotropy of source rocks: Implications for hydrocarbon generation and primary migration: AAPG Bulletin, **80**(4), 531−544.
Wu, X., Chapman, M., Li, X. Y., et al., 2012, Anisotropic elastic modelling for organic shales: 74th EAGE Conference and Exhibition.
Xu, S., and Payne, M. A., 2009, Modeling elastic properties in carbonate rocks: The Leading Edge, **28**(1), 66−74.
Zhu, Y., Xu, S., Payne, M., et al., 2012, Improved rock-physics model for shale gas reservoirs: 82th Annual International Meeting, SEG, Expanded Abstracts, 1−5.

Qian Ke-Ran is an engineer and a post-doctoral fellow from Petroleum Exploration and Production Research Institute of Sinopec. He received his Bachelor's degree from Yangtze University (2010), Master's degree from University of Edinburgh (2011), PhD degree from China University of Petroleum (Beijing) (2016). Currently, he works in Sinopec exploration and Development Research Institute. His research interests mainly focus on anisotropic rock physics modeling and sweet spot prediction of unconventional reservoirs.